Nanoscale

COMMUNICATION

View Article Online
View Journal | View Issue

Cite this: *Nanoscale*, 2015, **7**, 8361

Received 3rd March 2015,
Accepted 3rd April 2015

DOI: 10.1039/c5nr01391g

www.rsc.org/nanoscale

Design and synthesis of micron-sized spherical aggregates composed of hollow Fe_2O_3 nanospheres for use in lithium-ion batteries†

Jung Sang Cho, Young Jun Hong, Jong-Heun Lee and Yun Chan Kang*

A novel structure denoted a "hollow nanosphere aggregate" is synthesized by introducing nanoscale Kirkendall diffusion to the spray pyrolysis process. The hollow Fe_2O_3 nanosphere aggregates with spherical shape and micron size are synthesized as the first target material. A solid iron oxide–carbon composite powder that is prepared by a one-pot spray pyrolysis process is transformed into the hollow Fe_2O_3 nanosphere aggregates by sequential post-pyrolysis treatments under reducing and oxidizing atmospheres. The nanoscale Kirkendall diffusion plays a key role in the formation of the hollow Fe_2O_3 nanosphere aggregates with spherical shape and micron size. The unique structure of the hollow Fe_2O_3 nanosphere aggregates results in their superior electrochemical properties as an anode material for lithium ion batteries by improving the structural stability during cycling. The hollow metal oxide nanosphere aggregates with various compositions for wide applications including energy storage can be prepared by the simple fabrication method introduced in this study.

Introduction

To create rechargeable lithium-ion batteries (LIBs) with superior electrochemical properties, nanostructured transition metal oxide materials with high specific capacities, fast rate performances, and long cycle lives have been developed.[1–8] When used as energy storage materials, hollow metal oxide powders exhibit good electrochemical properties at high current densities because of their decreased diffusion length and the increased contact area between the electrolyte and electrode for Li^+ insertion/desertion.[9–13] Even though various types of hollow oxide materials have been studied as anode and cathode electrode materials for lithium secondary batteries, these hollow powders cannot be readily applied as battery materials because of their low energy density, which is due to their low tap density.[14–19]

Hollow nanopowders, consisting of particles several nanometers in size and with a low void volume, have the ideal structure for an anode material in LIBs because of their structural stability and volumetric energy density. Hollow nanopowders composed of ultrafine particles are mainly prepared by applying the Kirkendall effect to liquid solution methods.[20–26] First, a metal nanopowder is formed through the reduction of metal cations in an aqueous media. The nanopowder is then transformed into a hollow nanopowder through oxidation by the Kirkendall diffusion process under an oxygen-containing atmosphere. The initial metal nanopowder must have a dense structure to produce the hollow metal oxide nanopowder through Kirkendall diffusion. Therefore, there have been no reports of a fabrication method for hollow metal oxide nanopowders through Kirkendall diffusion that are not based on a liquid solution method. The sintering and particle growth of metal nanopowders that takes place before Kirkendall diffusion occurs and prevents the fabrication of hollow metal oxide nanopowders with no aggregation between the particles. Therefore, the development of a novel and simple synthesis process for hollow nanospheres remains a great challenge. In addition, hollow nanopowders composed of particles that are several nanometers in size cannot be applied efficiently as anode materials in LIBs because of the difficulties in handling nanopowders and achieving a high tap density.

Powders composed of micron-sized spherical particles are commonly used as anode materials in LIBs because of their high tap density and volumetric energy density.[27–31] However, micron-sized spherical particles with a solid structure have poor cycling and rate performances.[2,32–34] Therefore, micron-sized spherical aggregates of hollow nanospheres with a high structural stability have an ideal structure for commercial LIBs.

In this study, to the best of our knowledge, we fabricated micron-sized aggregates of hollow nanospheres for the first time. The Fe_2O_3 powder with a unique structure was prepared with a three-step process. A solid iron oxide–carbon composite

Department of Materials Science and Engineering, Korea University, Anam-Dong, Seongbuk-Gu, Seoul 136-713, Republic of Korea. E-mail: yckang@korea.ac.kr; Fax: +82-2-928-3584; Tel: +82-2-3290-3268

†Electronic supplementary information (ESI) available. See DOI: 10.1039/c5nr01391g

powder that was prepared with one-pot spray pyrolysis was transformed into the hollow Fe_2O_3 nanosphere aggregates by sequential post-pyrolysis treatments under reducing and oxidizing atmospheres. The formation mechanism of the aggregates and their electrochemical properties as anode materials in LIBs were investigated.

Results and discussion

The morphology of the FeO_x–carbon composite powder prepared directly with spray pyrolysis using the spray solution containing sucrose is shown in Fig. 1a. The particles are spherical in shape, have a smooth surface, and exhibit little aggregation. The polymerization and carbonization of sucrose under a nitrogen atmosphere forms the carbon-based material of the particles. A large amount of carbon-based material disturbed the crystal growth of the iron oxide formed through the decomposition of iron nitrate enneahydrate. Therefore, a FeO_x–carbon composite particle with an amorphous structure was formed from each droplet. The X-ray diffraction (XRD) shown in Fig. 1b shows the appearance of a broad peak between 20 and 25° which indicates the presence of amorphous carbon. The absence of extra peaks reveals the amorphous structure of the FeO_x–carbon composite powder. The carbon content of the FeO_x–carbon composite powder was estimated to be 51% from the TGA curve shown in Fig. 1c.

The reduction of the iron oxide uniformly embedded in the carbon network resulted in the formation of the Fe–carbon composite powder. The morphology of the Fe–carbon composite powder is shown in Fig. 2. The scanning electron microscopy (SEM) image shown in Fig. 2a displays the rough surface of the composite particles. The crystal growth of the iron has changed the smooth surface of the FeO_x–carbon composite particles into a rough surface. The transmission electron microscopy (TEM) images shown in Fig. 2b and c exhibit the dense structure of the Fe–carbon composite particles. The TEM and high-resolution TEM (HRTEM) images (Fig. 2c and d) show the iron nanocrystals embedded in the amorphous carbon matrix. The clear lattice fringes shown in Fig. 2d are separated by 0.2 nm, which corresponds to the (110) plane of

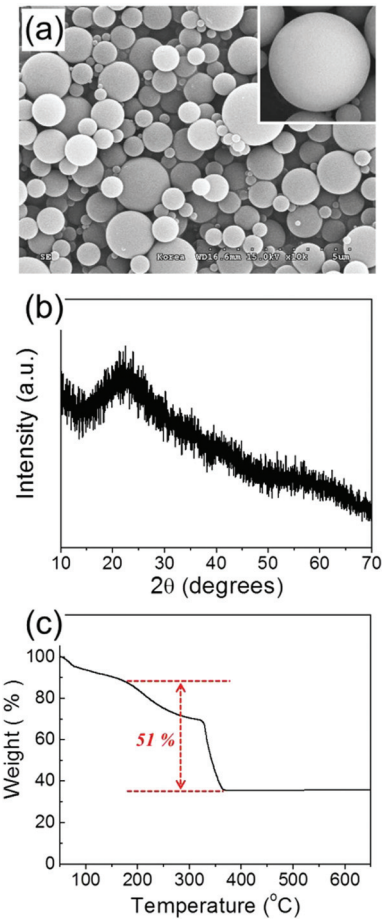

Fig. 1 (a) SEM image, (b) XRD pattern, and (c) TG curve of the as-synthesized FeO_x–carbon composite powders by spray pyrolysis.

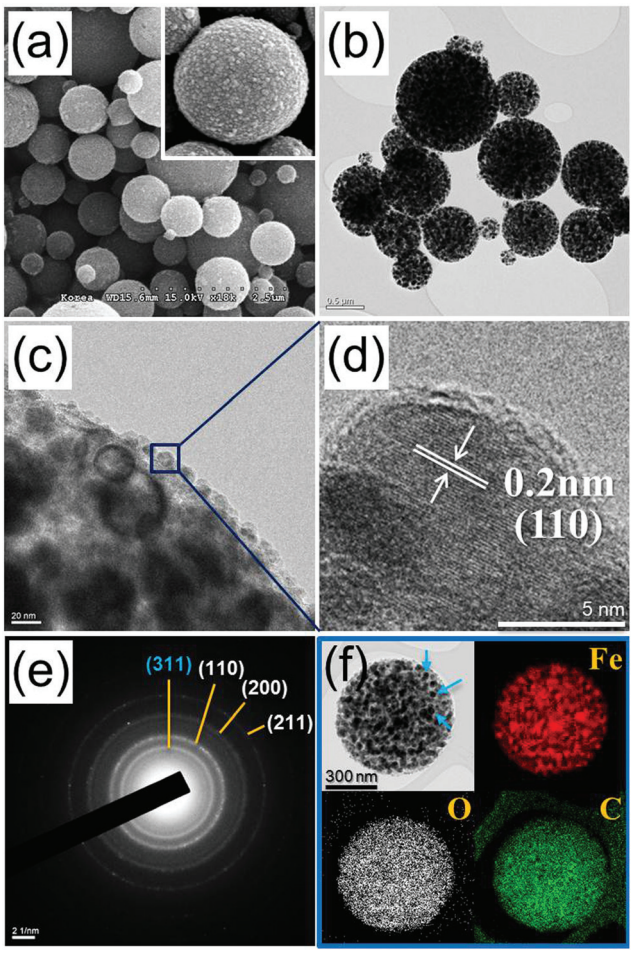

Fig. 2 Morphologies, SAED, and elemental mapping images of the Fe–carbon composite powder post-treated at 500 °C under a H_2/Ar mixed gas atmosphere: (a) SEM image, (b) and (c) TEM images, (d) HR-TEM image, (e) SAED pattern, and (f) elemental mapping images.

Fe. As can be seen in Fig. 2d, ultrafine Fe nanocrystals with a mean size of 20 nm have been dispersed across the surface of the composite particles. The reaction of hydrogen gas with the iron oxide first occurs at the surface of the composite particles. Therefore, Fe nanocrystals are initially formed on the surface of the composite particles in the early stages of the reduction process. Subsequently, the complete reduction of the inner core of the particles, as well as the effects of the Ostwald ripening process, results in the formation of Fe nanocrystals with a broad size distribution. The Fe nanocrystals are first formed during the early stage of the reduction process and grow into larger crystals through the Ostwald ripening process. Therefore, Fe nanocrystals that are smaller than 20 nm are dispersed inside the composite particles. The selected area electron diffraction (SAED) pattern shown in Fig. 2e reveals the presence of (110), (200), and (211) lattice planes corresponding to the Fe phase, as well as the (311) plane of the Fe_3O_4 phase due to the partial surface oxidation of Fe nanocrystals by exposure to air. The XRD pattern shown in Fig. S1a† reveals the complete reduction of the FeO_x–carbon composite into Fe–carbon composite by the reduction process. The mean crystallite size of the Fe nanocrystals calculated from the peak width of the XRD pattern is shown in Fig. S1a† using the Scherrer equation is 45 nm. The elemental mapping images (Fig. 2f) show the uniform distribution of Fe and C throughout the Fe–carbon composite particles. Visible Fe nanocrystals that were grown by the Ostwald ripening process are also present in the elemental mapping images, as indicated by the arrows.

The Fe–carbon composite powder was oxidized to form the uniquely structured Fe_2O_3 powder. The morphology of the Fe_2O_3 powder is shown in Fig. 3. The SEM and TEM images of the Fe_2O_3 particles (Fig. 3a and b, respectively) show that they have a similar morphology to that of the Fe–carbon composite particles. However, the inner structure of the Fe_2O_3 particles is not the same as that of the Fe–carbon composite particles. The TEM image (Fig. 3c) shows the aggregated structure of the hollow nanospheres. The Fe nanocrystals are converted into the hollow Fe_2O_3 nanospheres through the Kirkendall effect during the heat treatment. The clear lattice fringes shown in the inset of Fig. 3d are separated by 0.27 nm, which corresponds to the (104) plane of the α-Fe_2O_3 phase. The shell thickness of the hollow Fe_2O_3 nanospheres is about 4 nm, as determined from the TEM image shown in Fig. 3c. The broad peaks of the XRD pattern shown in Fig. S1b† are evidence of the ultrafine size of the Fe_2O_3 nanocrystals that form the hollow nanospheres. The selected area electron diffraction (SAED) pattern shown in Fig. 3e confirms the formation of α-Fe_2O_3. The oxidation of Fe into Fe_2O_3 is further supported by the XPS spectra shown in Fig. S2.† Only oxygenated functional groups, like C=O and O=C–O, are present in the O 1s peak of the Fe–carbon composite powder before undergoing the heat treatment. However, after the heat treatment, C=O and O=C–O groups disappear and the functional group corresponding to Fe–O bonding at 529 eV is newly present in the hollow Fe_2O_3 nanosphere aggregates. In the Fe 2p spectrum (Fig. S2c†), there are two peaks at binding energies of 711 eV for Fe $2p_{3/2}$ and 724 eV for Fe $2p_{1/2}$ and a shakeup satellite at 719 eV, which are the characteristic peaks of Fe(III) in α-Fe_2O_3.[35–38] No components related to zero-valent Fe and Fe^{2+} are observed. The graphitic carbon layers dispersed between the hollow nanospheres can be seen in the HRTEM image, as indicated by the arrows in Fig. 3d. A small amount of amorphous carbon was transformed into the graphitic carbon during the first stage of the post-pyrolysis treatment, with the iron acting as a catalyst. However, the elemental mapping images and TGA curve shown in Fig. 3f and S3,† respectively, suggest that the decomposition of almost all of the carbon-based material occurred during the formation of the hollow Fe_2O_3 nanosphere aggregates.

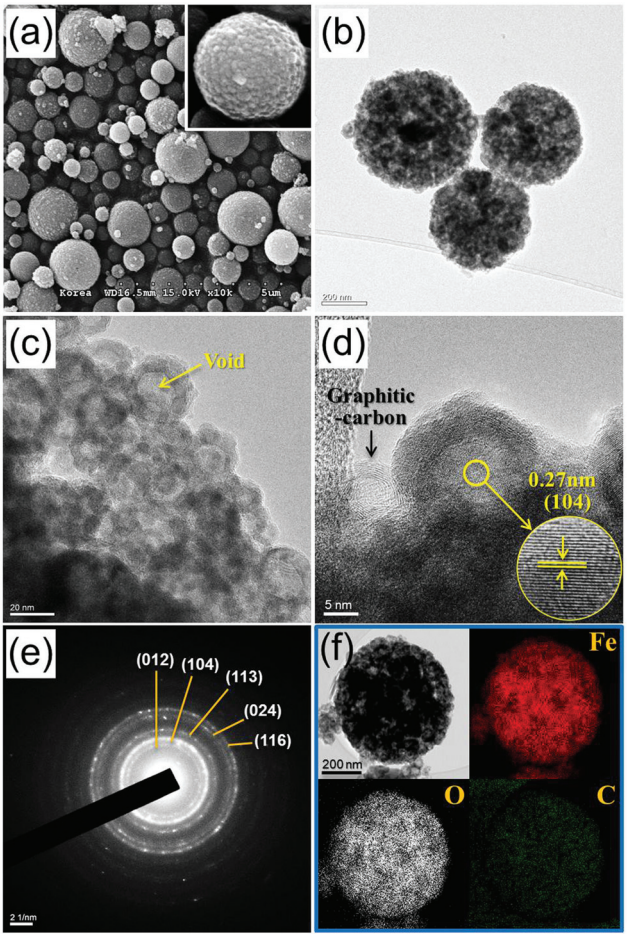

Fig. 3 Morphologies, SAED, and elemental mapping images of the hollow Fe_2O_3 nanosphere aggregates: (a) SEM image, (b) and (c) TEM images, (d) HR-TEM image, (e) SAED pattern, and (f) elemental mapping images.

A schematic of the formation mechanism of the hollow nanosphere aggregates is investigated in detail by tracing the changes in the particle morphology induced by the post-pyrolysis treatments and shown in Scheme 1. The FeO_x–carbon composite powder is prepared with one-pot spray pyrolysis. The FeO_x–carbon composite powder is formed from the drying of droplets, decomposition of iron nitrate enneahydrate, and

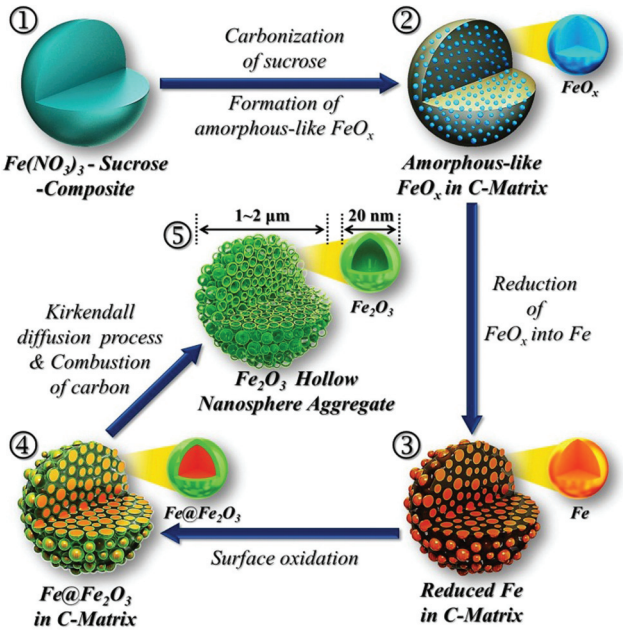

Scheme 1 Formation mechanism of the hollow Fe_2O_3 nanosphere aggregate by Kirkendall-type diffusion.

polymerization and carbonization of sucrose under a nitrogen atmosphere (Scheme 1-① and -②). The reduction of the FeO_x–carbon composite powder during the first stage of the post-pyrolysis treatment produces the Fe–carbon composite powder, in which Fe nanocrystals that are several tens of nanometers in size are uniformly distributed within the carbon microspheres (Scheme 1-③ and Scheme 2-①). The second stage of the post-pyrolysis treatment produces the hollow Fe_2O_3 nanosphere aggregates. The Fe nanocrystals are converted into hollow Fe_2O_3 nanospheres during this heating process by the Kirkendall effect. A thin Fe_2O_3 layer forms over the Fe nanocrystals through the partial oxidation of the nanocrystals' surface (Scheme 1-④ and Scheme 2-②). After the formation of the thin Fe_2O_3 layer, Fe cations diffuse outward from the boundary between the Fe and Fe_2O_3 layers to the surface of the Fe/Fe_2O_3 (core/shell) nanocrystals faster than oxygen can diffuse inward. The oxygen anion has a large ionic radius (140 pm), and therefore, has a slower diffusion rate through the Fe_2O_3 layer compared to the Fe cations, which have a small ionic radius (Fe^{2+} = 76 pm, Fe^{3+} = 65 pm). Accordingly, Kirkendall voids were generated near the Fe/Fe_2O_3 interface during vacancy-assisted exchange of the material *via* bulk interdiffusion (Scheme 2-③), which gives rise to coarsening and enhancement of pore growth in the spheres (Scheme 1-⑤ and Scheme 2-④). The complete conversion of Fe into Fe_2O_3 through Kirkendall-type diffusion transforms the Fe nanocrystals dispersed throughout the carbon matrix into Fe_2O_3 nanospheres. The amorphous carbon decomposes into carbon dioxide during the formation of the Fe_2O_3 nanospheres because of the oxidizing atmosphere. Consequently, the Fe–carbon composite powder is converted into the micron-sized hollow Fe_2O_3 nanosphere aggregates (Scheme 1-⑤).

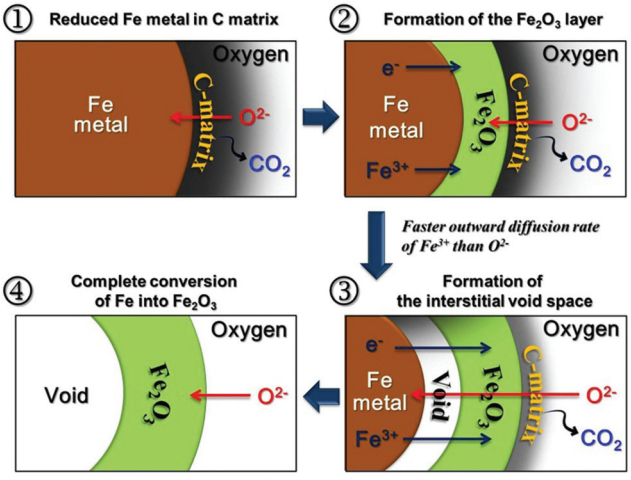

Scheme 2 Chemical conversion process in the surface region of a Fe sphere in C matrix.

The solid Fe_2O_3 powder was prepared directly with spray pyrolysis using a spray solution that did not contain sucrose. The SEM image shown in Fig. S4a† demonstrates the spherical shape of the particles and non-existent aggregation between the particles. The XRD pattern of this solid powder (Fig. S4b†) shows that it has a pure α-Fe_2O_3 structure, with no impurities. The N_2 adsorption and desorption isotherms as well as the Barrett–Joyner–Halenda (BJH) pore size distributions of the hollow Fe_2O_3 nanosphere aggregates and solid powder are shown in Fig. S5.† The hollow Fe_2O_3 nanosphere aggregate has well-developed micro- and meso-pores, with a pore diameter of 3 nm at the maximum of the distribution. However, the solid Fe_2O_3 powder has mesopores, with a pore diameter of 15 nm at the maximum of the distribution. The Brunauer–Emmett–Teller (BET) surface areas of the hollow Fe_2O_3 nanosphere aggregates and solid powder are 138 and 4 m^2 g^{-1}, respectively.

The electrochemical properties of the hollow Fe_2O_3 nanosphere aggregates and solid powder are shown in Fig. 4; the charge and discharge curves of the two samples at a constant current density of 3 A g^{-1} are shown in Fig. 4a and b. The initial discharge curve of the hollow Fe_2O_3 nanosphere aggregates shows two weak plateaus near 1.0 and 1.5 V because of the insertion of lithium into the α-Fe_2O_3 structure without any structural changes and a phase transformation from the hexagonal α-$Li_xFe_2O_3$ structure to the cubic $Li_xFe_2O_3$ structure, respectively.[1,39,40] However, the initial discharge curve of the solid Fe_2O_3 powder with a low BET surface area does not show the same plateaus near 1.0 and 1.5 V. The two samples have long plateaus near 0.7 V because of the complete reduction of Fe(III) to Fe(0), formation of Li_2O, and irreversible reduction reaction of the electrolyte to form a solid electrolyte interphase (SEI) film.[41–43] The initial discharge capacities of the hollow Fe_2O_3 nanosphere aggregates and solid powder are 1267 and

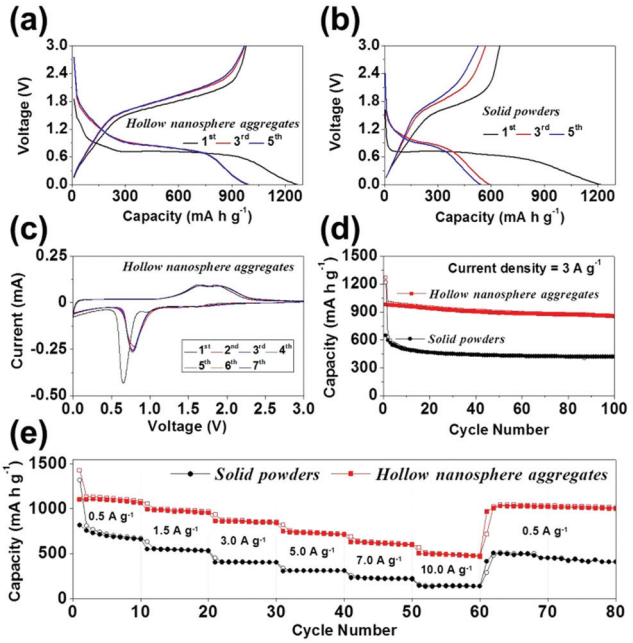

Fig. 4 Electrochemical properties of the solid Fe_2O_3 powders and hollow Fe_2O_3 nanosphere aggregates: (a) and (b) charge–discharge curves, (c) CV curves of hollow Fe_2O_3 nanosphere aggregates, (d) cycling performances, and (e) rate performances.

1216 mA h g^{-1} and their initial Coulombic efficiencies are 77 and 53%, respectively. The formation of an SEI layer on the surface of the powders and the incomplete restoration of metallic Fe during the initial charging process decreased the initial Coulombic efficiency of the two samples. In addition, the structural stability of the two samples during the first discharging and charging cycle caused the difference between their initial Coulombic efficiencies. The morphologies of the two samples obtained after the first cycle are shown in Fig. S6.† The solid Fe_2O_3 powder was broken into several pieces during the first discharging and charging processes. On the other hand, the spherical morphology of the hollow Fe_2O_3 nanosphere aggregates was completely maintained after first cycle. The cyclic voltammetry (CV) curves of the hollow Fe_2O_3 nanosphere aggregates for the first 7 cycles at a scan rate of 0.1 mV s^{-1} are shown in Fig. 4c. The sharp reduction peak observed at 0.7 V *vs.* Li^+/Li coincides well with the plateau observed in the initial discharge curve in Fig. 4a. The good overlapping of the CV curves from the second cycle onward reveals good reversibility of the electrochemical reactions. The different structural stabilities of the two samples affected their cycling performances. The hollow Fe_2O_3 nanosphere aggregates had similar charge and discharge capacities for the 3rd and 5th cycles, as shown in Fig. 4a. On the other hand, the solid Fe_2O_3 powders with unstable structure during insertion and desertion processes exhibit differences in their charge and discharge capacities for the 3rd and 5th cycles. The discharge capacities of the hollow Fe_2O_3 nanosphere aggregates and solid powder after 100 cycles at a current density of 3 A g^{-1} are 854 and 419 mA h g^{-1}, respectively. The rate performances of the two samples are shown in Fig. 4e, in which the current density was increased step-wise from 0.5 to 10 A g^{-1} and then decreased to 0.5 A g^{-1}. The hollow Fe_2O_3 nanosphere aggregates have a good rate performance and their high capacity is maintained when the current density is reduced back to 0.5 A g^{-1}. The stable reversible discharge capacities of the hollow Fe_2O_3 nanosphere aggregates decrease from 1084 to 505 mA h g^{-1} as the current density increases from 0.5 to 10 A g^{-1}. On the other hand, the capacities of the solid Fe_2O_3 powder decrease continuously, even after returning to the low current density of 0.5 A g^{-1}.

The Nyquist impedance plots of the hollow Fe_2O_3 nanosphere aggregates and solid powder before and after 1 and 50 cycles are shown in Fig. 5. The medium-frequency semicircles in the Nyquist plots of the electrodes were assigned to the charge-transfer resistance (R_{ct}).[2,44,45] The precise values of R_{ct} are calculated from a simulated equivalent circuit as described by Zheng *et al.*[46,47] The hollow Fe_2O_3 nanosphere aggregates

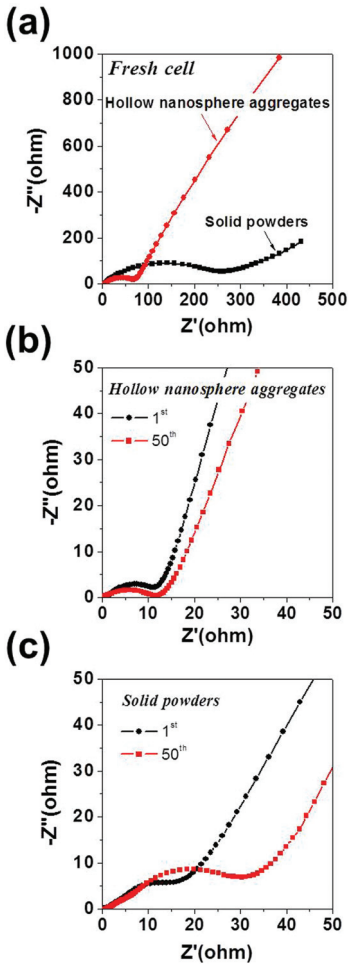

Fig. 5 Impedance analysis of the solid Fe_2O_3 powders and hollow Fe_2O_3 nanosphere aggregates: (a) before cycling, (b) after cycling of hollow Fe_2O_3 nanosphere aggregates, and (c) after cycling of solid Fe_2O_3 powders.

with graphitic carbon exhibit a lower R_{ct} of 69.8 Ω than 260.7 Ω of the solid Fe_2O_3 powder before cycling, as shown in Fig. 5a. The synergetic effect of hollow nanostructure and a graphitic carbon resulted in the low R_{ct} of the hollow Fe_2O_3 nanosphere aggregates. The hollow Fe_2O_3 nanosphere aggregates with graphitic carbon also exhibit a low R_{ct} of 12.6 and 13.1 Ω after 1st and 50th cycles, respectively, as shown in Fig. 5b. However, the R_{ct} of the solid Fe_2O_3 powder increases from 16.1 to 31.5 Ω as the number of cycles increases from 1st to 50th cycle, as shown in Fig. 5c. The morphologies of the two samples obtained after first 100 cycles are shown in Fig. S7.† The spherical morphology of the solid Fe_2O_3 cannot be found in the SEM image shown in Fig. S7a.† The large volume change during the repeated lithium insertion and desertion processes destroyed the spherical morphology of the solid Fe_2O_3 powders. However, the overall structure of the hollow Fe_2O_3 nanosphere aggregates is maintained even after repeated lithium insertions and desertions, as shown in Fig. S7b.† The void space of the hollow nanosphere accommodated the large volume change due to repeated lithium insertion and desertion processes.

Conclusions

A new preparation method for uniquely structured metal oxide microspheres that consist of aggregated hollow nanospheres was investigated. The hollow Fe_2O_3 nanosphere aggregates fabricated for the first time in this study were prepared from a FeO_x–carbon composite powder fabricated directly with spray pyrolysis by performing sequential post-pyrolysis treatments under reducing and oxidizing atmospheres. Nanoscale Kirkendall diffusion played a key role in the formation of the hollow Fe_2O_3 nanosphere aggregates. The micron-sized spherical aggregates of hollow nanospheres had high structural stability and an ideal structure for anode materials in LIBs, which undergo huge volume changes during the lithium insertion and desertion processes. In addition, hollow metal oxide nanosphere aggregates with various compositions could be prepared with the simple fabrication method introduced in this study. Therefore, hollow metal oxide nanosphere aggregates could be applied to a wide range of fields, including energy storage.

Acknowledgements

This work was supported by the Creative Industrial Technology Development Program (10045141) funded By the Ministry of Trade, Industry & Energy (MI, Korea).

Notes and references

1 J. Chen, L. N. Xu, W. Y. Li and X. L. Gou, *Adv. Mater.*, 2005, **17**, 582–586.
2 Y. J. Hong, M. Y. Son and Y. C. Kang, *Adv. Mater.*, 2013, **25**, 2279–2283.
3 J. Jiang, Y. Li, J. Liu, X. Huang, C. Yuan and X. W. Lou, *Adv. Mater.*, 2012, **24**, 5166–5180.
4 Y. Li, B. Tan and Y. Wu, *Nano Lett.*, 2008, **8**, 265–270.
5 H. Wang, L. F. Cui, Y. Yang, H. Sanchez Casalongue, J. T. Robinson, Y. Liang, Y. Cui and H. Dai, *J. Am. Chem. Soc.*, 2010, **132**, 13978–13980.
6 L. Mai, L. Xu, C. Han, X. Xu, Y. Luo, S. Zhao and Y. Zhao, *Nano Lett.*, 2010, **10**, 4750–4755.
7 C. K. Chan, X. F. Zhang and Y. Cui, *Nano Lett.*, 2008, **8**, 307–309.
8 J. Yan, E. Khoo, A. Sumboja and P. S. Lee, *ACS Nano*, 2010, **4**, 4247–4255.
9 Y. Yao, M. T. McDowell, I. Ryu, H. Wu, N. Liu, L. Hu, W. D. Nix and Y. Cui, *Nano Lett.*, 2011, **11**, 2949–2954.
10 N. S. Ergang, M. A. Fierke, Z. Wang, W. H. Smyrl and A. Stein, *J. Electrochem. Soc.*, 2007, **154**, A1135–A1139.
11 C. Niu, J. Meng, C. Han, K. Zhao, M. Yan and L. Mai, *Nano Lett.*, 2014, **14**, 2873–2878.
12 J. Lian, X. Duan, J. Ma, P. Peng, T. Kim and W. Zheng, *ACS Nano*, 2009, **3**, 3749–3761.
13 A. Vu, Y. Qian and A. Stein, *Adv. Energy Mater.*, 2012, **2**, 1056–1085.
14 Q. Xie, F. Li, H. Guo, L. Wang, Y. Chen, G. Yue and D. L. Peng, *ACS Appl. Mater. Interfaces*, 2013, **5**, 5508–5517.
15 C. Delacourt, P. Poizot, S. Levasseur and C. Masquelier, *Electrochem. Solid-State Lett.*, 2006, **9**, A352–A355.
16 J. Gao, J. Ying, C. Jiang and C. Wan, *J. Power Sources*, 2007, **166**, 255–259.
17 H. J. Guo, Q. H. Li, X. H. Li, Z. X. Wang and W. J. Peng, *Energy Convers. Manage.*, 2011, **52**, 2009–2014.
18 S. W. Oh, H. J. Bang, S. T. Myung, Y. C. Bae, S. M. Lee and Y. K. Sun, *J. Electrochem. Soc.*, 2008, **155**, A414–A420.
19 X. Lou and Y. Zhang, *J. Mater. Chem.*, 2011, **21**, 4156–4160.
20 R. K. Chiang and R. T. Chiang, *Inorg. Chem.*, 2007, **46**, 369–371.
21 H. J. Fan, U. Gösele and M. Zacharias, *Small*, 2007, **3**, 1660–1671.
22 H. J. Fan, M. Knez, R. Scholz, D. Hesse, K. Nielsch, M. Zacharias and U. Gösele, *Nano Lett.*, 2007, **7**, 993–997.
23 L. Hu, N. Yan, Q. Chen, P. Zhang, H. Zhong, X. Zheng, Y. Li and X. Hu, *Chem. – Eur. J.*, 2012, **18**, 8971–8977.
24 S. Jana, J. W. Chang and R. M. Rioux, *Nano Lett.*, 2013, **13**, 3618–3625.
25 G. Xiao, Y. Zeng, Y. Jiang, J. Ning, W. Zheng, B. Liu, X. Chen, G. Zou and B. Zou, *Small*, 2013, **9**, 793–799.
26 Y. Yin, R. M. Rioux, C. K. Erdonmez, S. Hughes, G. A. Somorjai and A. P. Alivisatos, *Science*, 2004, **304**, 711–714.
27 H. G. Jung, J. Kim, B. Scrosati and Y. K. Sun, *J. Power Sources*, 2011, **196**, 7763–7766.
28 S. M. Oh, J. Y. Hwang, C. S. Yoon, J. Lu, K. Amine, I. Belharouak and Y. K. Sun, *ACS Appl. Mater. Interfaces*, 2014, **6**, 11295–11301.

29 Y. Wen, Y. Zhu, A. Langrock, A. Manivannan, S. H. Ehrman and C. Wang, *Small*, 2013, **9**, 2810–2816.
30 L. Wu, J. Lu and S. Zhong, *J. Solid State Electrochem.*, 2013, **17**, 2235–2241.
31 X. Zhang, H. Guo, X. Li, Z. Wang and L. Wu, *Electrochim. Acta*, 2012, **64**, 65–70.
32 H. Kim and J. Cho, *Chem. Mater.*, 2008, **20**, 1679–1681.
33 Y. N. Ko, S. B. Park, K. Y. Jung and Y. C. Kang, *Nano Lett.*, 2013, **13**, 5462–5466.
34 M. Y. Son, Y. J. Hong, J. K. Lee and Y. C. Kang, *Nanoscale*, 2013, **5**, 11592–11597.
35 M. F. Hassan, M. M. Rahman, Z. P. Guo, Z. X. Chen and H. K. Liu, *Electrochim. Acta*, 2010, **55**, 5006–5013.
36 K. Karthikeyan, S. Amaresh, S. N. Lee, V. Aravindan and Y. S. Lee, *Chem. – Asian J.*, 2014, **9**, 852–857.
37 G. Wang, Y. Ling, D. A. Wheeler, K. E. George, K. Horsley, C. Heske, J. Z. Zhang and Y. Li, *Nano Lett.*, 2011, **11**, 3503–3509.
38 P. Yang, Y. Ding, Z. Lin, Z. Chen, Y. Li, P. Qiang, M. Ebrahimi, W. Mai, C. P. Wong and Z. L. Wang, *Nano Lett.*, 2014, **14**, 731–736.
39 S. Yuan, Z. Zhou and G. Li, *CrystEngComm*, 2011, **13**, 4709–4713.
40 F. Han, D. Li, W. C. Li, C. Lei, Q. Sun and A. H. Lu, *Adv. Funct. Mater.*, 2013, **23**, 1692–1700.
41 D. Deng, M. G. Kim, J. Y. Lee and J. Cho, *Energy Environ. Sci.*, 2009, **2**, 818–837.
42 M. Reddy, T. Yu, C. H. Sow, Z. X. Shen, C. T. Lim, G. Subba Rao and B. Chowdari, *Adv. Funct. Mater.*, 2007, **17**, 2792–2799.
43 G. Zhou, D. W. Wang, F. Li, L. Zhang, N. Li, Z. S. Wu, L. Wen, G. Q. Lu and H. M. Cheng, *Chem. Mater.*, 2010, **22**, 5306–5313.
44 S. M. Lee, S. H. Choi and Y. C. Kang, *Chem. – Eur. J.*, 2014, **20**, 15203–15207.
45 N. Li, G. Liu, C. Zhen, F. Li, L. Zhang and H. M. Cheng, *Adv. Funct. Mater.*, 2011, **21**, 1717–1722.
46 H. Wu, M. Xu, H. Wu, J. Xu, Y. Wang, Z. Peng and G. Zheng, *J. Mater. Chem.*, 2012, **22**, 19821–19825.
47 H. Wu, M. Xu, Y. Wang and G. Zheng, *Nano Res.*, 2013, **6**, 167–173.